Fuel 375 (2024) 132504

Contents lists available at ScienceDirect

Fuel

journal homepage: www.elsevier.com/locate/fuel

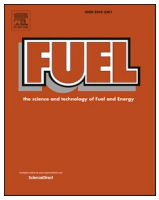

Full Length Article

Quantitative three-dimensional reconstruction of cellular flame area for spherical hydrogen-air flames

Gengxin Zhang [a], Hongming Xu [a,*], Dawei Wu [a], Junfeng Yang [b], Mohamed E. Morsy [b], Mehdi Jangi [a], Roger Cracknell [c]

[a] Department of Mechanical Engineering, School of Engineering, University of Birmingham, Edgbaston, Birmingham B15 2TT, UK
[b] School of Mechanical Engineering, University of Leeds, Leeds LS2 9JT, UK
[c] Shell Global Solutions UK, Shell Centre, London SE1 7NA, UK

ARTICLE INFO

Keywords:
Hydrogen
Premixed combustion
Instability
Spherical flame
3D reconstruction
Cellular factor

ABSTRACT

The cellular flame area continues to increase with the development of cells on the spherical flame surface, which will greatly promote the flame burning rate and propagation speed. This work mainly focuses on a new three-dimensional (3D) reconstruction method of the cellular structure on the flame surface, attempting to quantitatively characterize the real flame area. Initially, the visualization investigation of hydrogen-air premixed spherical flames within a constant volume vessel was conducted using the Schlieren optical technique under room temperature and atmospheric pressure conditions. In parallel, the Cellpose 2.0 graphical user interface was used for the preliminary training of the cell segmentation model. Subsequently, this pre-trained model was applied in the image post-processing, enabling the quantitative characteristics extraction of the cellular structure, such as the cells number, area, and the flame radius, etc. Additionally, a concept of peak height h on the flame profile was proposed to characterize the fluctuation degree of flame profile. A new flame equivalent radius r_u was defined by the average value of valid distance from flame centroid to flame profile pixel by pixel. Based on the comparison of cell equivalent radius r and average peak height $\overline{h}$, an innovative 3D reconstruction concept was proposed for the quantitative characterization of flame area. Finally, cellularity factor ξ was introduced to evaluate the cellularization degree on spherical flames surface. Results show that the appearance of secondary cracks marks the formal onset of flame cellularization, accompanied by an increase in the $\overline{h}$. In the later stages of flame development, cellularization will eventually tend to a stable value of about 0.4, indicating the occurrence of "saturated state". After 3D reconstruction, the average cell area stable at around 26 mm^2 in this stage. The results of this study provide data support for the construction of combustion models in the field of premixed hydrogen-air combustion.

1. Introduction

In the context of carbon neutrality, the development and application of zero-carbon fuels become particularly critical. Especially, hydrogen, with its zero-emission combustion properties, plays an important role in promoting the transformation of the energy structure [1–3]. As we know, challenges, such as low energy density, storage and transportation issues, and safety risks associated with flammability and explosiveness, remain significant barriers in the widespread application of hydrogen energy [4]. In a variety of application scenarios, the potential of hydrogen as a fuel for internal combustion engines (ICEs) is gradually becoming apparent [5]. However, the behavior of hydrogen-air flames within combustion chambers may be affected by the instability of cellular structures, resulting in a range of phenomena such as combustion oscillations, flame acceleration, and potentially explosive scenarios, which in turn affects the engine's combustion rate, efficiency and emissions [6,7]. Therefore, a study of flame acceleration propagation is of vital importance for the design, application, and risk assessment of hydrogen-fueled engines, as well as other combustion equipment.

In fact, the intrinsic instability of premixed flames, including thermal diffusion instability, hydrodynamic instability, and buoyancy instability, play a crucial role in influencing the propagation and burning speed of flames, and the cellular structure on the flame surface is a major representation of such instabilities [8,9]. In the past, researchers are

* Corresponding author.
E-mail address: h.m.xu@bham.ac.uk (H. Xu).

https://doi.org/10.1016/j.fuel.2024.132504
Received 12 March 2024; Received in revised form 26 June 2024; Accepted 11 July 2024
Available online 21 July 2024

Nomenclature

ICEs	internal combustion engines
3D	three-dimensional
DNS	direct numerical simulations
2D	two-dimensional
GUI	graphical user interface
CVV	constant volume vessel
ER	equivalence ratios
LED	light emitting diode
HSV	high-speed video camera
T	time after ignition
ROIs	regions of interest
r_u	equivalent flame radius
O	flame centroid (origin)
M_{min}	minimum wave trough position
R_{min}	distance from flame centroid O to wave trough M_{min}
m	peaks number
$P_1, P_2, P_3, \cdots, P_i, \cdots, P_m$	successive peaks position
$R_1, R_2, R_3, \cdots, R_i, \cdots, R_m$	distances from flame centroid O to peaks position
$h_1, h_2, h_3, \cdots, h_i, \cdots, h_m$	peak height
$\overline{h}$	average peak height
r	equivalent cell radius
n	cells number
$r_1, r_2, r_3, \cdots, r_i, \cdots, r_n$	cells radius of cell from number 1 to n
r_1	sample cell radius
r_{large}	large-scale cell
r_{small}	small-scale cell
S_1	raw flame image plane
S_2	perpendicular to the raw flame image plane
S_3	tangential plane on spherical flame surface
$O_1, O_2, O_3, \cdots, O_i, \cdots, O_n$	cells centroid of cell from number 1 to n
O_1	sample cell centroid
O_1'	O_1 projected onto sphere surface with radius R_{min}
O_1''	extend the line $O - O_1'$ by a distance $\overline{h}$
A_1	intersection point closer to O where the line $O - O_1'$ intersects the equivalent circle of the sample cell
B_1	intersection point farther to O where the line $O - O_1'$ intersects the equivalent circle of the sample cell
A_2	A_1 vertically projected onto sphere surface with radius R_{min}
B_2	B_1 vertically projected onto sphere surface with radius R_{min}
O_2	center of the projected spherical crown of the sample cell
D	enclosed sample cell region
S	actual cell area
$Q\ (x, y, z)$	a mapping point on sphere surface with radius $R_{min} + \overline{h}$
α	angle formed where line $O - O_1'$ intersects with plane S_1 ($<90°$)
β	angle formed where line $A_2 - O_2$ intersects with plane S_1 ($<90°$)
γ	angle formed where line $O - Q$ intersects with plane S_1 ($<90°$)
dAp	actual mapping area of the projection pixels in region D
$d\varsigma$	projected pixels area
r_{cl}	critical radius
A_c	flame surface area obtained through image processing
A_f	surface area of the laminar flame
ξ	cellularity factor

attempting to extract the cellular structure information displayed on the spherical flame surface through various experimental and simulation methods, and then to analyze the flame propagation speed. Until now, the spherical premixed combustion flame propagation of various fuels and multi-component mixed gases has been extensively studied [10–15]. Yang et al. have clearly identified three developmental stages in the flame propagation process using normalized flame speed and flame radius, including the cell smoothing expansion, transition, and relative saturation stage. It can be seen that the flame surface area increases rapidly with the number of cells during the transition stage, leading to a rapidly acceleration of the flame [16]. Ranga Dinesh et al. used three-dimensional (3D) direct numerical simulations (DNS) to study the structure and propagation of lean premixed high hydrogen content − carbon monoxide syngas flames under different initial turbulence levels. The results showed that under high-pressure turbulent conditions, the flame develops cellular burning structures and are superimposed with flame wrinkles caused by turbulence. The highly wrinkled cells formed on the surface of spherical flames increase their area, thus increasing the global propagation speed under high pressure [17]. Moreover, the quantitative characterization of the cellular structure on the flame surface cannot be separated from image processing analysis. The cell segmentation model in the image processing program is a crucial factor affecting the reliability of the analysis results [18,19]. Zuo et al. conducted a quantitative study on the cell instability and self-acceleration characteristics of premixed C1-C3 alkane-air mixtures using spherical expanding flames, proposing the concept of cell density to characterize the degree of flame cellularization. The results showed that under the strongest conditions of cell instability, the cell instability of these three alkane-air mixtures increases with the increase in the number of carbon atoms in the fuel, but the cell density does not increase indefinitely [20,21]. Recently, Yin et al. proposed a method for approximating the segmentation radius to quantitatively analyze the cellular structure of three high-component alkanes flames. To facilitate computation, they made some assumptions about partial extraction in the extraction of cell numbers [22]. In addition to the direct background subtraction and adaptive thresholding for binarization, which are used for cell segmentation and feature extraction, the recent application of the watershed algorithm proposed by Xu et al. has also achieved good results in cell segmentation [23,24]. However, the traditional image processing techniques commonly used above face many challenges in cell boundary extraction, such as sensitivity to noise and high impact on subjective consciousness [25]. Research suggests that deep learning has potential in handling the challenges of cell segmentation [26]. It is noteworthy that Cellpose, a deep learning-based method, has been introduced and is extensively used for cell segmentation in biology and medicine [27–29]. Currently, the application of this algorithm is still at the initial exploration stage in the field of combustion, particularly in the context of cell segmentation and feature extraction on the surface of spherical hydrogen-air flames. Furthermore, some studies have directly utilized image processing techniques to quantitatively extract two-dimensional (2D) cell sizes from schlieren images. Kim et al. quantitatively analyzed cell sizes in a local position of flame images, finding that cells caused by thermal diffusion instability presented smaller sizes [30]. Wu et al. defined the 2D average cell area as a parameter for assessing flame instability. It is noted that flame instability slightly decreases after complete cellularization, and that increasing the proportion of hydrogen in the mixture enhances the flame cellularization [31]. Similarly, Li et al. also viewed the cell in 2D and used image processing technology to quantitatively obtain the cells number and the average cells area on the flame surface, which were then used to describe the instability of the flame [32]. However, it is evident that the above studies overlook the fact that the cell area obtained from 2D schlieren images is smaller than the actual cell area.

In order to obtain more accurate quantitative information of the

cellular structure on the spherical flames surface, the process of 3D reconstruction of the cell structure is also crucial. The Future Engines and Fuels Lab at the University of Birmingham was the first research institute to propose the concept of quantitatively reconstructing the real flame structure [33]. Subsequently, Huang et al. performed a 3D reconstruction on the crack length, considering that the cell sizes in cellularization flames are usually on the same level, they were simplified to ideal circles with the same radius. Then a meaningful parameter was derived, the average cell radius, from the total crack length, but its definition formula overlooked the cells number, and both the cell area and perimeter were projected onto the surface of a smooth fitted sphere with the equivalent flame radius [34,35]. Later on, Li et al. utilized the concept of projection to achieve the 3D reconstruction of cell areas. They carried out a series of quantitative extractions of cellular features such as crack length, cell number, and average cell area for ethyl acetate premixed flames [36]. Following this, they utilized this method to conduct a series of studies on the spherical flame propagation of different component alternative fuels [37,38]. However, the direct projection and mapping relationships involved in this 3D reconstruction make it difficult to fully reproduce the real characteristics of the cell structure because of differences in cell size, leaving considerable space for improvement in this field of research.

From the above literature review, it is clear that more accurate quantitative 3D reconstruction of the flame surface area is worth further study. Therefore, this paper proposes an innovative concept of 3D cell area reconstruction for analyzing the cellular structure on the surface of spherical premixed hydrogen-air flames. The structure of this study is organized in the following: Initially, the Cellpose 2.0 graphical user interface (GUI), based on the deep learning algorithms, is utilized for the training of the cell segmentation model in our work. Following this, the pre-trained model is applied to analyze the cellular structure present on the flame surface. This analysis yields vital data regarding the cellular structure, encompassing the number and average size of cells. Subsequently, a new definition for the equivalent flame radius considering flame buoyancy and the average peak height of the flame front was proposed. Based on the comparison of equivalent cell radius and average peak height, the core concept of 3D cell area reconstruction is introduced. Finally, the cellularity factor is further derived using the improved cell area computational model, which can be used in an optimized model to characterize flame propagation speed. The quantitative 3D reconstruction method of cellular flame area proposed in this study are expected to contribute to flame propagation speed prediction, which can promote further development in the field of efficient and safe hydrogen engine design.

2. Experimental equipment and method

2.1. Optical system arrangement and experimental conditions

As shown in the Fig. 1, the premixed combustion experiments were conducted inside a spherical constant-volume vessel (CVV). High-speed schlieren optical arrangement were employed during these experiments to capture the spherical hydrogen-air flame. Further details regarding the experimental setup are elaborated in the earlier work [39]. It is mainly focused on the innovative concept of 3D reconstruction of cellular flame areas in this work. Therefore, the experimental parameters remained consistent, including the initial conditions like room temperature, atmospheric ambient pressure, and a fuel–air equivalence ratio (ER) of 0.8, to ensure comprehensive observation of the full flame cellularization process. Meanwhile, three tests were conducted under the same conditions, and the average value was taken as the final result to ensure the reliability of the results of this work.

Fig. 2 presents a detailed visualization of the morphological evolution of hydrogen-air premixed flames at ER0.8. Here presents four distinct moments. Specifically, the occurrence of secondary cracks is identified at 1.9 ms, while 2.6 ms is considered the moment corresponding to the critical radius r_{cl} because the flame imagery gradually exhibits a uniform distribution of numerous cellular structures post this timeframe. The emergence of these abundant cells can be attributed to the interplay of thermal diffusion and hydrodynamic instabilities. Generally, due to the constraints of spatial scale, with buoyancy instability being of negligible impact in this scenario due to spatial scale limitations [16]. More quantitative cellular flame information obtaining on the flame surface requires further image processing below.

2.2. Image processing process

Cellpose, a publicly available code hosted on Github, has emerged as a pivotal instrument in the realm of image analysis, which is particularly influential in areas necessitating intricate analysis of cellular structures [40]. Within combustion science, the adoption of Cellpose represents an innovative approach to flame image analysis, which cannot be found in any publications by other institutes until to now. The utilization of algorithms grounded in deep learning within Cellpose is anticipated to enhance the accuracy of cellular segmentation in these studies, marking a significant advancement in the relevant field.

Fig. 3 illustrates the utilization of the Cellpose 2.0 GUI for the development of customized models, fundamentally based on the concept of an 'interactive machine learning loop' that synergizes human expertise with algorithmic processing [41]. The integration of human input in this loop unfolds as follows: (1) Start with a selected initial model from "model zoo" and setting an assumed cell diameter for the training; (2) Import a raw premixed spherical flame image into the system; (3) Begin the training and initial outcomes may require improvement because poor result segmentation first time, prompting manual corrections such as adding the regions of interest (ROIs) corresponding to presumed cell locations; (4) Subsequent to these adjustments, the model undergoes further training based on prior inputs to develop a customized model; (5) As the number of training cycles increases, the number of manual ROIs added in each cycle gradually

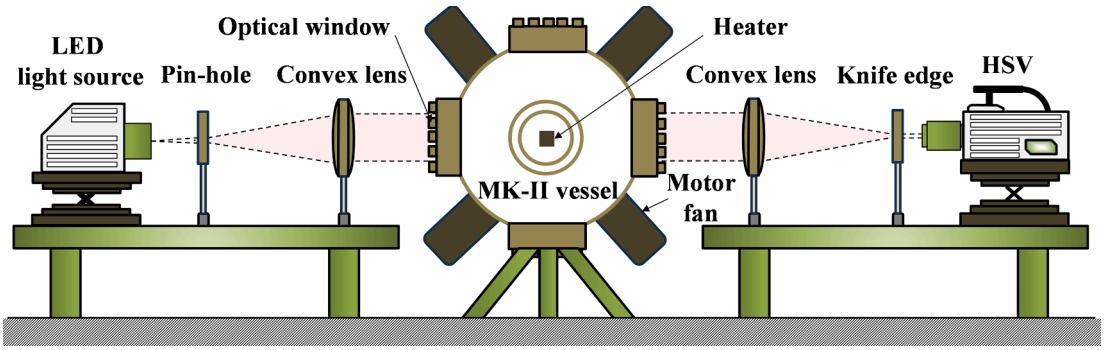

Fig. 1. Schlieren arrangement for the premixed combustion of hydrogen-air.

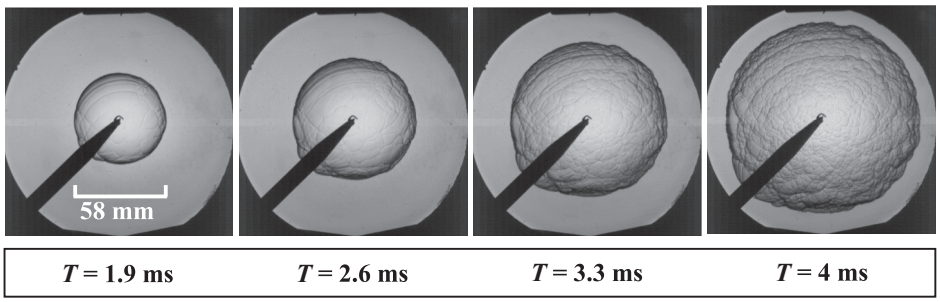

Fig. 2. Morphology evolution of hydrogen-air premixed flame [300 K/0.1 MPa/ER0.8].

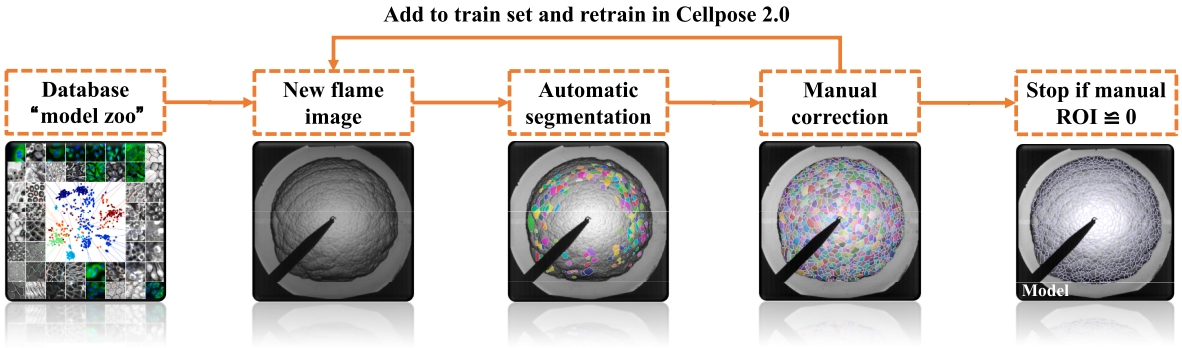

Fig. 3. Cell segmentation model pretraining process using Cellpose 2.0 GUI.

decreases even to zero, the customized model will reach a stage where it is adept at identifying and segmenting cellular structures within flame images.

Based on the principle of identifying the maximum cell number, extensive testing has ultimately confirmed that "CPx" is the initial model with the best performance in the "model zoo". Generally, the average precision (AP) can be used to assess the level of cell segmentation, serving as a crucial parameter for validation. Therefore, a program for the calculation of AP was developed in our previous work [41]. Results show that the final AP reached 0.625, which meets the high standards for cell segmentation in the field of biology [42]. This also indicates that the cell identification accuracy of our developed deep-learning cell segmentation model is high. Future work can directly utilize this pre-trained cell segmentation model from this study to train on other spherical cell flame images, thereby significantly enhancing the training efficiency in the field of combustion.

As illustrated in Fig. 4, the diagram showcases a comprehensive process for image processing, including the import of a pre-trained cell segmentation model. The process begins with a series of preprocessing operations applied to the original flame images, primarily involving background reduction, contrast and brightness enhancement, and noise reduction. Moreover, the Otsu method is utilized for the automatic thresholding of the flame images, converting them into binary format. Additionally, morphological closing is applied to these binary images to mitigate the impact of the ignition device on the extraction of flame contours. Finally, the extracted flame contours are superimposed onto the original image using green contour lines for easy visualization.

After the above image processing, information about cells and flames can be obtained, such as the labeling of the cell centroid, the cells number, equivalent radius and average area, flame equivalent radius and outline information, etc., which provides the sufficient data support for the subsequent 3D reconstruction of the spherical flame area. It is noted that the region obscured by the ignition device, indicated by the angle between the two orange color lines (the 36° angle of device vicinity from 120° to 156°, accounting for 10 % of the total), is excluded from post-processing considerations for avoiding the influence of the ignition device.

2.3. Three-dimensional reconstruction process for spherical flame

The 2D flame images captured using the schlieren technique lack the depth information of the 3D flame structure. To address this, a novel 3D reconstruction idea is proposed for that more accurate and quantitative 3D reconstructed spherical flame area as below.

2.3.1. Definitions of feature parameters: Average peak height ($\bar{h}$), equivalent flame radius (r_u), and cell scale

Before the introduce of the novel 3D reconstruction idea, some crucial parameters will be proposed and defined firstly. Fig. 5 (a) lays out the evolution of flame profiles, while Fig. 5 (b) defines the crucial parameters, the average peak heights ($\bar{h}$), for analyzing flame topography. The process begins by identifying the flame centroid O of the cellularized flame front at a given timing, which is then designated as the coordinate origin. Starting from the centroid O, the nearest distance to the flame profile is determined as R_{min}, marking the intersection point with flame profile as M_{min} (minimum wave trough position). Subsequently, all the successive peaks point $(P_1, P_2, P_3, \cdots, P_i, \cdots, P_m)$ on the flame profile are also clockwise identified from M_{min}, and their respective distances from the centroid O to each peak are labeled as $R_1, R_2, R_3, \cdots, R_i, \cdots, R_m$. Here, m is the peaks number on the flame profile. Unlike the previous definitions of flame radius, the flame radius proposed in this work considers the effect of slight flame buoyancy [43]. Specifically, the equivalent flame radius (r_u) is defined as the average distance from the flame centroid O to all pixel points along the flame profile, starting at the point M_{min} and moving clockwise pixel by pixel. By subtracting the minimum distance R_{min} from each distance to a peak, the height of each peak can be obtained as $h_1, h_2, h_3, \cdots, h_i, \cdots, h_m$ The average peak height $\bar{h}$ is therefore expressed as Equation (1) below. Additionally, in order to distinguish different planes in the following definitions, the plane where the 2D schlieren flame image is designated as S_1.

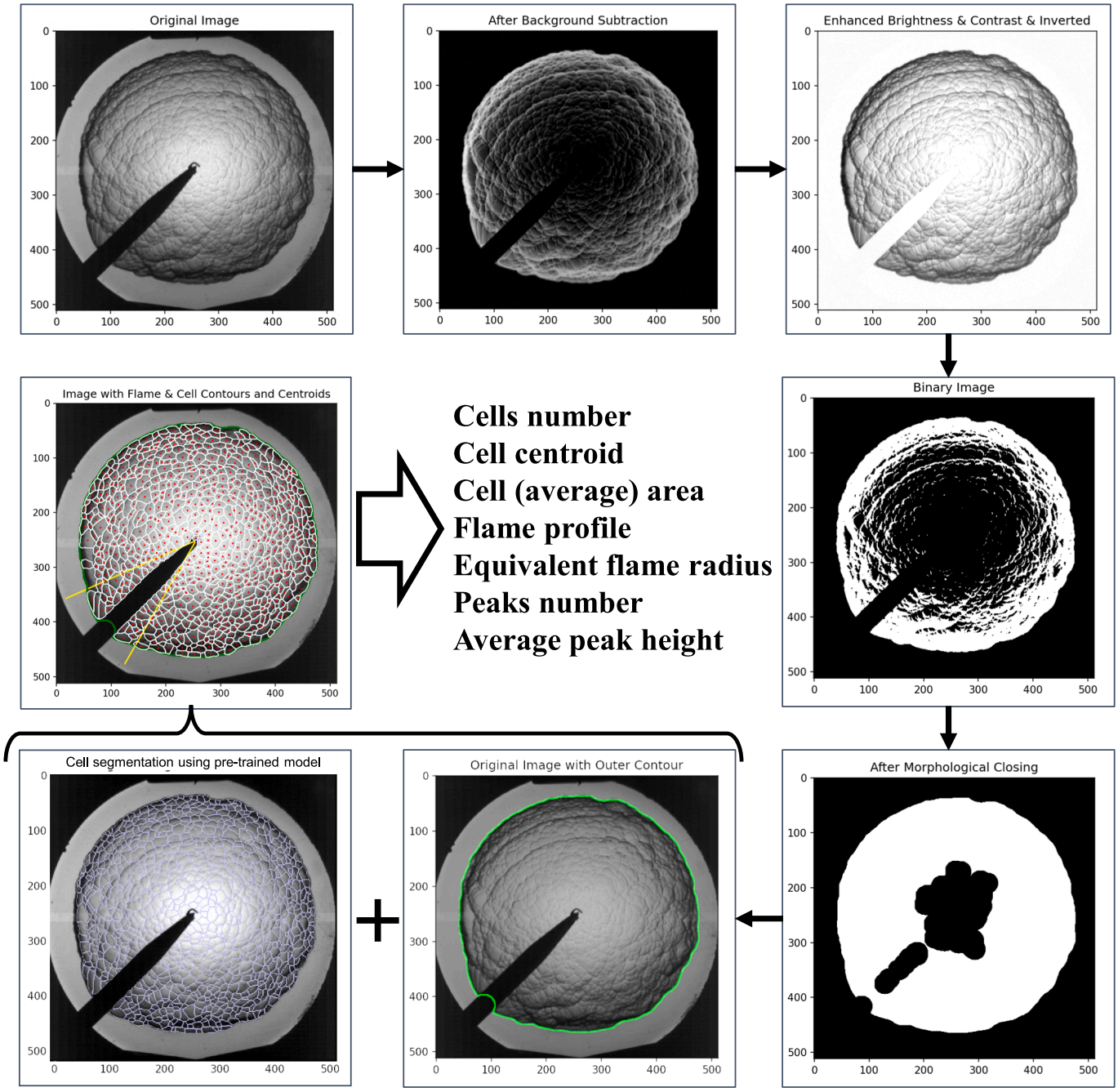

Fig. 4. Image processing process based pre-trained model using Cellpose 2.0 GUI.

$$\begin{aligned}\overline{h} &= (h_1 + h_2 + h_3 + \cdots + h_i + \cdots + h_m)/m \\ &= ((R_1 - R_{min}) + (R_2 - R_{min}) + (R_3 - R_{min}) + \cdots + (R_i - R_{min}) + \cdots \\ &\quad + (R_m - R_{min}))/m\end{aligned} \tag{1}$$

Fig. 6 illustrates the definition and differences of cell scales. As shown in this figure, the cell equivalent radius (r) is the radius of a circle with the same pixels number as the cells segmented by the image process program. Based on the average peak height $\overline{h}$ and the identified cell equivalent radius r proposed, the concept of cell scale was proposed as well. When the cell equivalent radius r is greater than or equal to the average crest height $\overline{h}$ ($r_{large} \geq \overline{h}$), the cell is named as a large-scale cell with a larger equivalent radius r_{large}; when the cell equivalent radius r is less than the average peak height $\overline{h}$ ($r_{small} < \overline{h}$), the cell is named as a small-scale cell with a smaller equivalent radius r_{small}.

2.3.2. 3D reconstruction of cell area based on the scale difference

According to the classification of different cell scales in Fig. 6, the novelty 3D cell area reconstruction ideas of large-scale cells and small-scale cells will be introduced in detail in this section. Before that, limited by the current Schlieren optical diagnostic setup captures spherical hydrogen-air flame imagery from a fixed direction, a hypothesis should be mentioned that flame images captured from various directions will exhibit similar flame profiles as shown in Fig. 5 (a), characterized by uniform average peak heights as defined in Fig. 5 (b) in different directions. Simultaneously, we hypothesize that each cell on the flame surface represents a spherical cap of a sphere with different radius, which means a flatter cell corresponds to a sphere with a larger radius. As depicted in Fig. 7 (a), the spherical cap area calculation

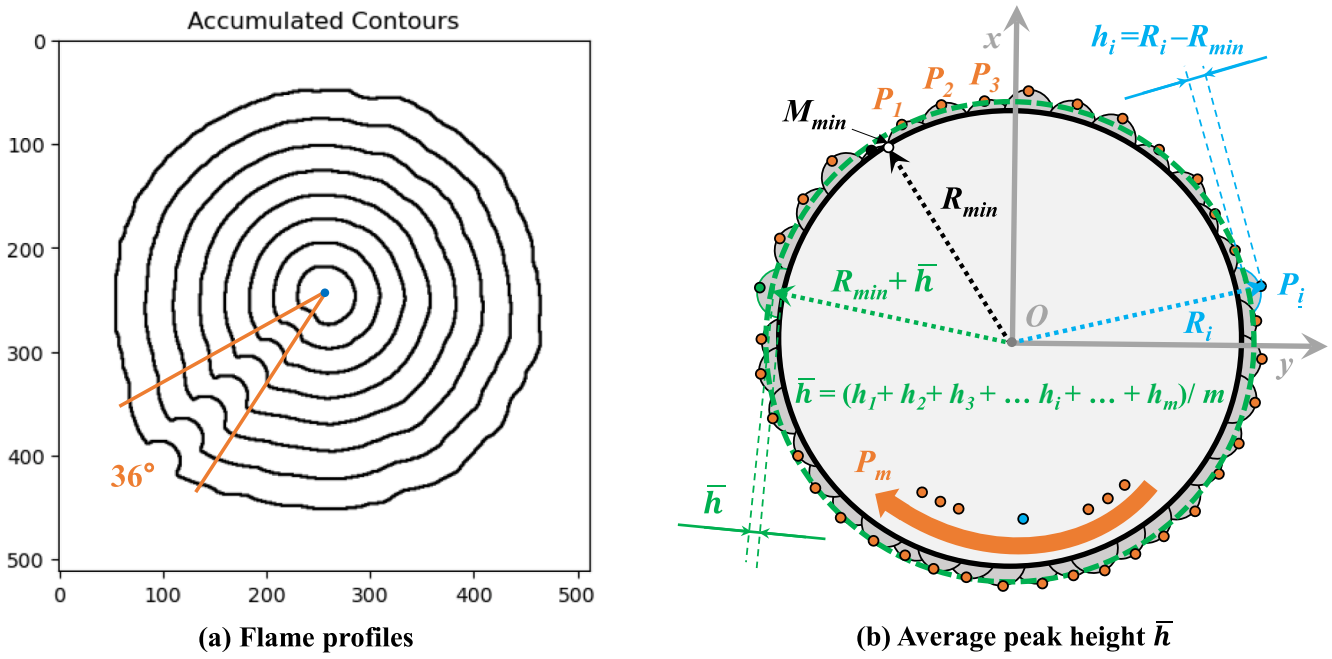

Fig. 5. (a) Evolution of flame profiles and (b) definitions of average peak height ($\bar{h}$).

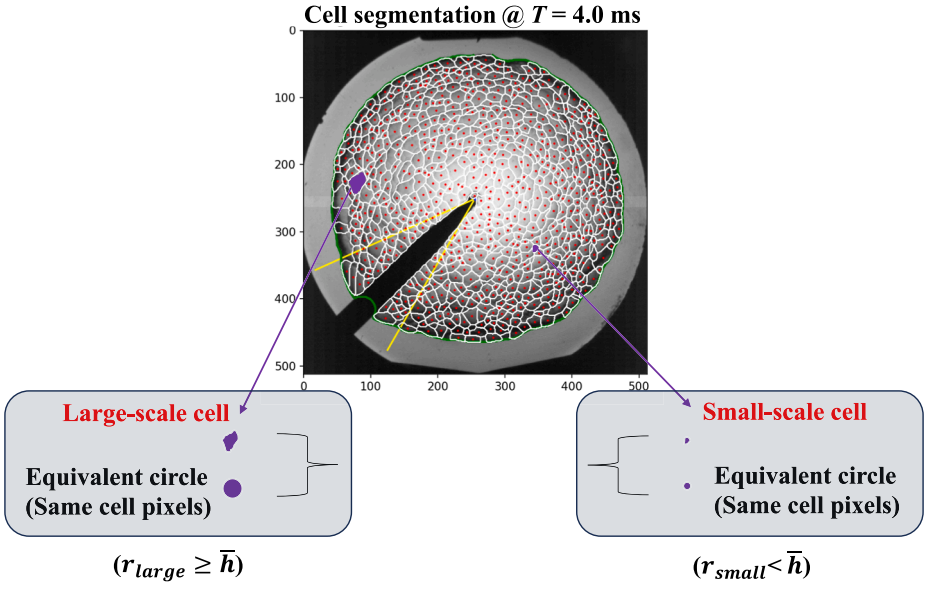

Fig. 6. Definition of cell equivalent radius (**r**) and the difference of cell scales.

formula is employed to resolve large scale cells ($r_{large} \geq \bar{h}$), and the sphere radius for all projections is R_{min} at this case. In contrast, Fig. 7 (b) demonstrates that smaller cells ($r_{small} < \bar{h}$) are directly projected onto the tangential plane of the sphere representing the flame with the flame radius $R_{min} + \bar{h}$ and be calculated through the idea of integrals.

From the initial image processing described in Section 2.2, all 2D cells number, location, perimeter, area and average area can be ascertained. A moving coordinate system wherein the *y*-axis invariably intersects the centroid of any cell scale, regardless of its position, are established. And then the centroid coordinates for all cells are determined (noting that *x* and *z* are invariably zero) and labeled as $O_1, O_2, O_3, \cdots, O_n$, while also calculating the equivalent radius of their respective circles as $r_1, r_2, r_3, \cdots, r_n$. Here, *n* is the recognized cells number on the flame surface.

Taking a small cell with radius r_1 as a sample cell, it is easy to find the point A_1 (closer to the center *O*) and the point B_1 (farther away from the center *O*) at both ends of the sample cell equivalent circle where the straight line intersects the O_1 of the cell centroid and the coordinate origin *O*. The subsequent key step is the dimensionality reduction via projection. A plane S_2 perpendicular to the flame surface S_1 is constructed passing through the coordinate origin *O* and the sample cell centroid O_1. The projection then bifurcates into two scenarios as below:

(1) As depicted in Fig. 7 (a), for $r_1 \geq \bar{h}$, which can be called large-scale cell, the cell centroid O_1 and the endpoints A_1 and B_1 are vertically projected onto the circular boundary with center *O* and radius R_{min} on vertical plane S_2, yielding projected points O_1', A_2, and B_2. Extending the line from the coordinate origin *O* through

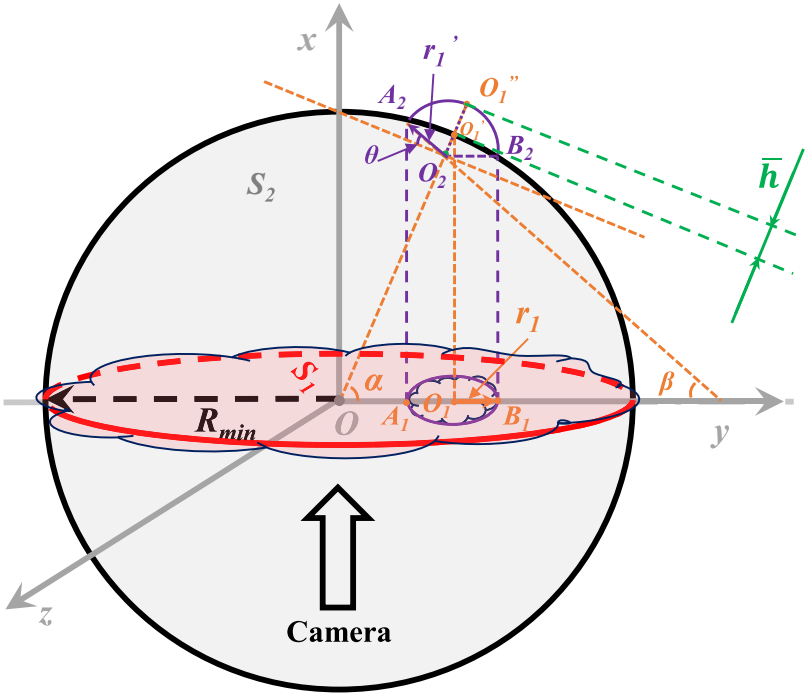

(a) 3D reconstruction of large-scale cell
($r_{large} \geq \bar{h}$)

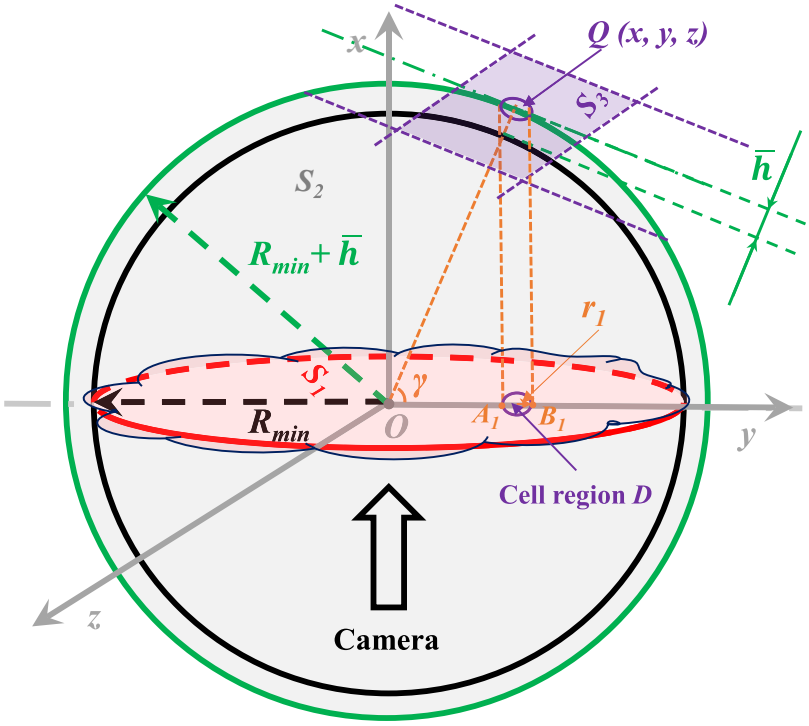

(b) 3D reconstruction of small-scale cell
($r_{small} < \bar{h}$)

Fig. 7. Three-dimensional reconstruction of cell area for various cell scale.

the projected centroid O_1' by a distance $\overline{h}$ reaches point O_1'', determining its coordinate and the angle α (less than 90°) with the horizontal plane S_1. With known coordinates of points A_2, B_2, and O_1'', and then the coordinates of the projected cell center O_2 and its radius r_1' can be deduced. The line connecting A_2 to O_2 and its extension defines the angle β (less than 90°) with plane S_1. For this case, the cell area after 3D reconstruction can be expressed as Equation (2).

$$S = 2\pi r_1'^{*} r_1'(1 - \sin((\alpha + \beta) - 90^o)) \quad (2)$$

(2) As depicted in Fig. 7 (b), for $r_1 < \overline{h}$, which can be called small-scale cell, assuming the Q (x, y, z) denotes a point on the 3D sphere surface characterized by an equivalent flame radius $R_{min} + \overline{h}$, which also represents the mapping of a point within an enclosed cell region D onto the spherical surface. The coordinates of the mapping point Q (x, y, z) on the 3D spherical surface for any point within the enclosed cell region D can be ascertained using Equation (3).

$$z^2 = r_u^2 - x^2 - y^2 \quad (3)$$

Furthermore, the cosine of the angle $(90^\circ - \gamma)$ between the tangent plane S_3 at mapping point Q (x, y, z) and the projection plane S_1 can be calculated using Equation (4) [36]:

$$\cos(90^\circ - \gamma) = \frac{1}{\sqrt{1 + \left(\frac{\partial z}{\partial x}\right)^2 + \left(\frac{\partial z}{\partial y}\right)^2}} \quad (4)$$

When the pixels in the enclosed cell region D are small enough, $d\zeta = dApcos(90^\circ - \gamma)$. dAp is the actual mapping area of the projection pixels in the region D and $d\zeta$ is the projected pixels area, respectively. Thus, the actual cell area S corresponding to the enclosed cell region D can be calculated as Equation (5):

$$S = \sum_D \sqrt{1 + \left(\frac{\partial z}{\partial x}\right)^2 + \left(\frac{\partial z}{\partial y}\right)^2} d\zeta \quad (5)$$

Similar procedures are applied to all other cells based on their equivalent radius r, and then the novel 3D reconstruction cell area can be obtained in this work.

2.4. Uncertainty statement

The uncertainty analysis in this work regarding the wrinkled flame area mainly involves two main aspects: the inaccuracy of cell information extraction after segmentation, including the accuracy of the trained cell segmentation model and the uncertainty in the number of cells during image processing, which has been analyzed in our previous work [41]. The second aspect is the inherent inaccuracies in the proposed 3D reconstruction of cell areas due to assumptions made during this process. These assumptions include: (1) the distribution probability of cells on the flame surface is the same from different viewing angles; (2) all cells have a certain height; and (3) the subjective setting of average peak height as the criterion for distinguishing between small and large scale of cells. Additionally, uncertainties arise from optical measurement errors and the random propagation caused by flame instability. All these factors contribute to the overall uncertainty in the final calculation of the wrinkled flame area. To minimize experimental uncertainties, we conducted the experiments three times under the same conditions to obtain an average value.

3. Results and discussion

3.1. Valid distance from flame centroid to profile and equivalent flame radius (r_u)

Fig. 8 (a) depicts the evolution of valid distances at four distinct timing, tracking from the minimum distance R_{min} from the flame centroid O to its profile, and following pixel by pixel along the flame profile. The valid distance here means within the valid angle range excluding the ignition device region (120°-156°) mentioned in the Section 2.2. As the flame develops, an increase in valid distance is observed along the y axis, indicating the flame radius is expanding over time. Horizontally, there is a gradual increase in the number of profile pixels, suggesting a growing flame perimeter over time. Additionally, the evolution curves of the valid distances highlight the magnification of the flame fractal characteristics, revealing more pronounced fluctuations. Interestingly, despite some fluctuations, the results show that the valid distance first increases and then decreases with the change of position on the flame profile. This suggests that one side of the flame profile is farther from the flame centroid while the opposite side is closer. Additionally, the image processing program detected that the position of the minimum distance M_{min} occurs at the lower side of the flame image, which implies that the observed phenomenon above may be due to a slight buoyancy effect during the flame propagation.

By averaging all valid distances at the same timing, as defined in the Section 2.3.1, the results of flame radius are obtained in Fig. 8 (b). The flame radius exhibits a generally linear growth, with the final radius constrained to approximately 62 mm due to the limitations of the CVV optical window. Moreover, raw flame images at key timing are annotated in the figure as well. Initial cracks appear at $T = 0.8$ ms, secondary cracks at $T = 1.9$ ms, and the critical radius of the flame is reached at $T = 2.6$ ms.

3.2. Valid peaks number (m) and the average peak height ($\overline{h}$)

Fig. 9 depicts the trajectory of average peak heights $\overline{h}$ and valid peaks number (m) over time on the left and right axis, respectively. The number of valid peaks here refers to the peaks that fall within the valid angle range (outside the range of 120° to 156°). Meanwhile, a filter condition is applied, requiring that the pixels difference between the two consecutive peaks should greater than 4 (approximately 1 mm). In the initial stages of ignition, energy fluctuations induce quite a degree of flame deformation (the position movement of centroids), which is a manifestation of the combustion system's transient response to the sudden influx of energy and the consequent establishment of a thermal gradient, resulting in a larger average peak height [44]. With the appearance of secondary cracks, when the flame radius reaches 29.55 mm, the flame centroid stabilizes with no further movement, and the average peak height shows a slight increased tendency, a result of continuous flame cellularization. The number of valid peaks also exhibits a marked increase in the later stages of flame development, which is also corroborated by Fig. 8 (a). This may be attributed to increased pulsations as the flame approaches the CVV walls [45,46].

3.3. Cells number (n) and the average cell area

Fig. 10 (a) presents the temporal record of the cells number identified through image processing proposed in this study, already corrected for the influence of the ignition device (increased by 10 %). At the beginning, the number of identified cells is quite small due to the incomplete formation of the cells. With the flame propagations, there is a continuous increase in the number of cells with two distinct surges. The first surge occurs after the appearance of secondary cracks, that is, when the flame radius reaches 29.55 mm at $T = 1.9$ ms. The second, more rapid, increase in cells number follows the flame radius exceeding the critical radius of

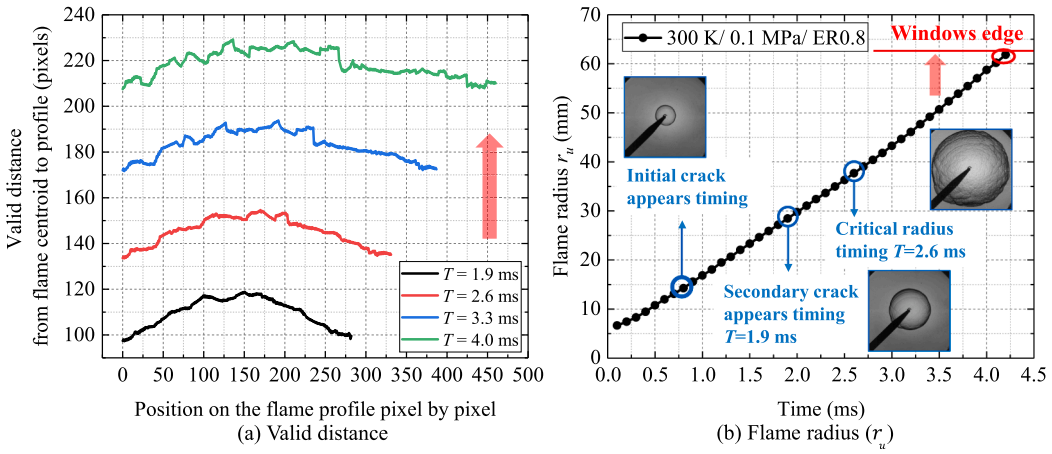

Fig. 8. Valid distance from flame centroid to profile pixel to pixel and equivalent flame radius (r_u).

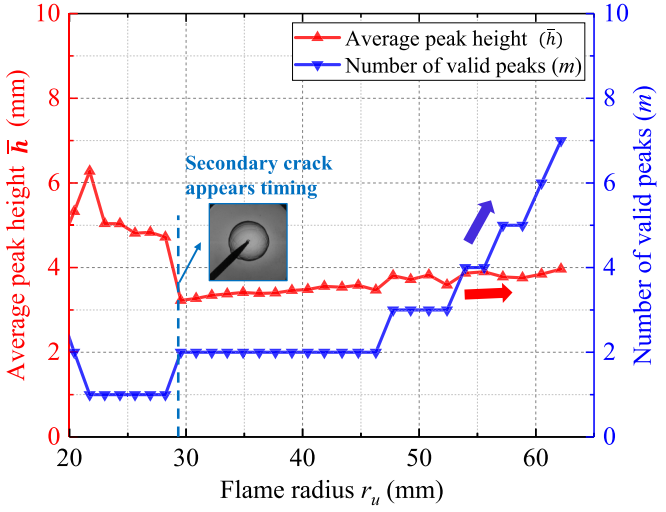

Fig. 9. Number of valid peaks (m) and average peak height ($\bar{h}$).

39.08 mm at T = 2.6 ms. The emergence of numerous cells after this timing enhances flame instability, which in turn promotes further division of cells. Fig. 10 (b) contrasts the evolution of the average cell area in 2D and 3D reconstructions as the flame development. Notably, the average cell area observed increases after 3D reconstruction compared to the 2D results. As the spherical flame grows beyond the critical radius, a significant reduction in average cell area in both 2D and 3D reconstructions is observed, likely due to the substantial increase in the number of cells on the flame surface. Eventually, the average cell area approaches a relatively constant value, indicating that the cellularization of the flame has reached a dynamic equilibrium. It is noteworthy that the 2D cell area stabilizes at around 14 mm^2, equivalent to an average 2D cell diameter of approximately 4.22 mm. In contrast, the estimated stable value for the average area of 3D cells gradually settles at around 26 mm^2.

3.4. Evaluation of spherical flame cellularization

The cellularity factor ξ proposed by Askari et al. can be used to evaluate the effect of cell formation on flame surface area and burning speed, which can be calculated using Equation (6) below [47]:

$$\xi = \frac{A_c}{A_f} - 1 \tag{6}$$

where A_c is the total area of irregular cells, which is the flame surface area obtained through our own image processing code developed in this work. A_f is the surface area of the laminar flame.

Fig. 11 (a) illustrates the difference between the laminar flame area and the wrinkled flame area after cellularization. Typically, the wrinkled flame area is larger than that of the laminar flame. However, the result shows that the wrinkled flame area is smaller in the early stages of

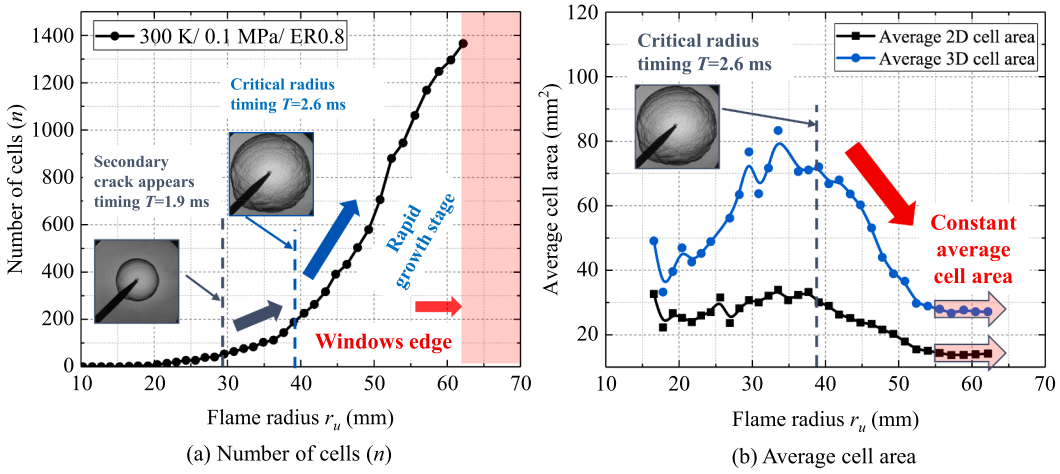

Fig. 10. Variations of cells number and average 2D & 3D cell area.

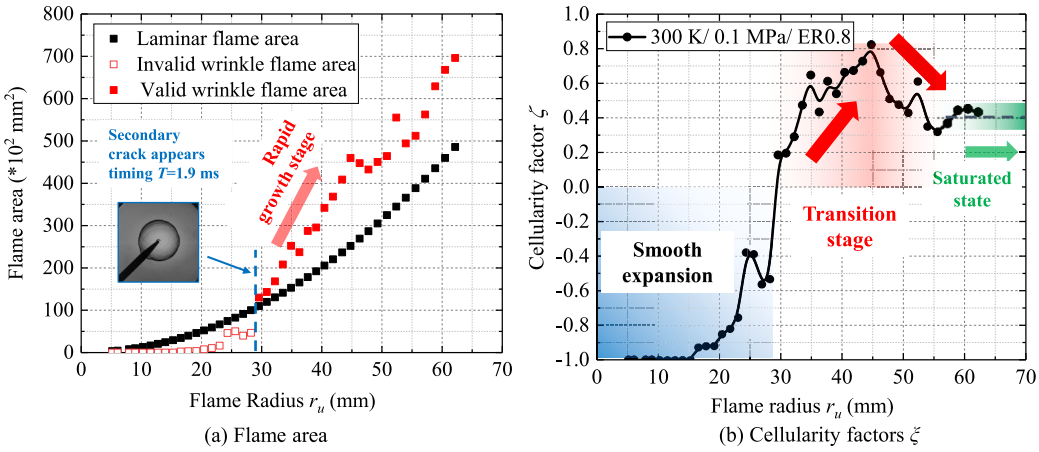

Fig. 11. Evaluation of spherical flame cellularization.

flame propagation. This is because not all the cells have fully formed at this stage, resulting in a smaller identified cells number and thus a smaller 3D reconstructed wrinkled flame area. Once secondary cracks occur, when the flame radius reaches 29.55 mm at $T = 1.9$ ms, a rapid increase in the wrinkled flame area can be clearly observed, surpassing the area of the laminar flame.

Fig. 11 (b) presents an analytical perspective on the temporal trends of the cellularity factor ξ. Yang et al. proposed that the development of flames will go through three stages: smooth expansion, transition and saturated state [16]. In fact, it is noted that the cellularization factor ξ essentially undergoes four stages based on the results of this study because of the transition stage can also be divided into an ascending stage and a descending stage. In the beginning, the spherical flame is marked by susceptibility to ignition disturbances, meanwhile, as mentioned above, it should be considered that not all the cells can be identified in the initial "smooth expansion stage", leading the cellularity factor ξ smaller than 0, which can be considered negligible and is covered by the light blue region in the graph. When the cell factor is greater than 0, it is deemed effective. It can be seen that the wrinkled flame area exceeds that of the laminar flame following the appearance of secondary cracks, at which point the cellularity factor ξ undergoes a jump in growth. As the flame expands and the flame is destabilized in the "transition stage", the cellularity factor ξ steadily climbs. After the flame develops beyond the critical radius for a certain period, the cellularity factor ξ experiences a slight decline, which can be contributed to the cellular structure on the flame surface gradually becomes saturated. Finally, the cellularity factor ξ approximately stabilizes at a constant average value of 0.4. This period correlates with a stabilization in the average cell area, suggesting a "saturated state" of cellularization, indicative of a state of dynamic equilibrium for the flame.

4. Conclusions

The quantitative 3D reconstruction of the cell area on the spherical flame surface contributes to the development of flame propagation speed model. In this work, an innovative 3D reconstruction method of cell area was proposed based on the cell scale difference and used for quantitative cellularization analysis of spherical hydrogen-air flames. Meanwhile, it should be mentioned that the Cellpose 2.0 GUI employed in our work is benefit for cell segmentation on the flame surface. The detailed results obtained are as follows.

(1) The valid distances from the flame centroid to the boundary contours demonstrates that the extent of flame spread upwards is broader than downwards, which may be caused by the effect of slight buoyancy on the flame propagation. Meanwhile, the flame equivalent radius obtained based on the average value of all valid distances shows an almost linear growth with time, and the final reach to 62 mm due to the limitation of optical window.

(2) After the emergence of secondary cracks at $T = 1.9$ ms, there is a slight upward trend in average peak height, which is a result of the flame continual cellularization. Additionally, the number of valid peaks shows a significant increase in the later stages, which may be attributed to the increased pulsations as the flame approaches the CVV walls.

(3) When the equivalent flame radius exceeds the critical radius of 39.08 mm at $T = 2.6$ ms, the rate of flame cellularization accelerates, leading to a rapid increase in the cells number and a swift decrease in the average cell area. Eventually, as the flame reaches a dynamic equilibrium state, the average area of the cells remains constant despite the continual increase in the cells number. Based on the 3D reconstructions, the average cell area increases and eventually stabilizing at around 26 mm^2.

(4) The cellularization factor ξ essentially undergoes three stages based on the flame propagation. In the initial "smooth expansion stage", cells are not yet fully formed, resulting in a negative value. Continuous cellularization occurs following the emergence of secondary cracks at $T = 1.9$ ms in the "transition stage", and the wrinkled flame area keeps increasing, causing a rapid rise in the ξ. But in the later stages of flame development, cellularity factor ξ shows a decrease after exceeding the critical radius some while and eventually stabilizes at an average value of 0.4, which can be attributed to the "saturated state" of flame cellularization.

Based on the new 3D reconstruct idea proposed in this work, future research will focus on conducting comparative analyses of the cellular structure evolution during the self-acceleration phase of spherical premixed hydrogen-air flames under a range of experimental conditions, including the variations in initial pressures, temperatures, and equivalence ratios, etc.

CRediT authorship contribution statement

Gengxin Zhang: Writing – original draft, Visualization, Validation, Software, Methodology, Investigation, Formal analysis, Data curation, Conceptualization. **Hongming Xu:** Writing – review & editing, Validation, Supervision, Project administration, Investigation, Funding acquisition. **Dawei Wu:** Writing – review & editing, Validation, Supervision, Project administration, Investigation. **Junfeng Yang:** Writing – review & editing, Validation, Resources, Project administration, Investigation. **Mohamed E. Morsy:** Validation, Resources, Investigation. **Mehdi Jangi:** Validation, Investigation. **Roger Cracknell:** Validation, Investigation.

Declaration of competing interest

The authors declare that they have no known competing financial interests or personal relationships that could have appeared to influence the work reported in this paper.

Data availability

Data will be made available on request.

Acknowledgements

The authors would like to acknowledge the EPSRC (Engineering and Physical Sciences Research Council, United Kingdom) for the financial support of the project 'Premixed Combustion Flame Instability Characteristics' (Grant No. EP/W002299/1). Additionally, thanks to Professor Wookyung Kim of Hiroshima University for providing the cellularization hydrogen-air flame images, which were used for training the deep learning cell segmentation model in this work.

References

[1] IEA. The Future of Hydrogen; 2019. Available from: https://www.iea.org/reports/the-future-of-hydrogen [accessed January 10 2024].
[2] Jin Y, Luo H, Zhang G, Zhai C, Ogata Y, Matsumura Y, et al. Ignition timing effect on the combustion performance of hydrogen addition in methane fermentation gas in a local energy system. Fuel 2022;324:124714.
[3] Chen D, Li J, Li X, Deng L, He Z, Huang H, et al. Study on combustion characteristics of hydrogen addition on ammonia flame at a porous burner. Energy 2023;263:125613.
[4] Abohamzeh E, Salehi F, Sheikholeslami M, Abbassi R, Khan F. Review of hydrogen safety during storage, transmission, and applications processes. J Loss Prev Process Ind 2021;72:104569.
[5] Verhelst S, Wallner T. Hydrogen-fueled internal combustion engines. Prog Energy Combust Sci 2009;35(6):490–527.
[6] Chen P, Ta S, Xie Y, Su X. Initial flame propagation characteristics of the hydrogen spherical premixed flame. Int J Hydrogen Energy 2023;48(92):36112–21.
[7] Reyes M, Tinaut FV, Horrillo A, Lafuente A. Experimental characterization of burning velocities of premixed methane-air and hydrogen-air mixtures in a constant volume combustion bomb at moderate pressure and temperature. Appl Therm Eng 2018;130:684–97.
[8] Wang G, Li Y, Li L, Qi F. Experimental and theoretical investigation on cellular instability of methanol/air flames. Fuel 2018;225:95–103.
[9] Li Y, Bi M, Zhang S, Jiang H, Gan B, Gao W. Dynamic couplings of hydrogen/air flame morphology and explosion pressure evolution in the spherical chamber. Int J Hydrogen Energy 2018;43(4):2503–13.
[10] Xie Y, Wang X, Bi H, Yuan Y, Wang J, Huang Z, et al. A comprehensive review on laminar spherically premixed flame propagation of syngas. Fuel Process Technol 2018;181:97–114.
[11] Oppong F, Luo Z, Li X, Song Y, Xu C. Intrinsic instability of different fuels spherically expanding flames: A review. Fuel Process Technol 2022;234:107325.
[12] Li Y, Xu W, Jiang Y, Liew KM. Effects of diluents on laminar burning velocity and cellular instability of 2-methyltetrahydrofuran-air flames. Fuel 2022;308:121974.
[13] Yin L, Xu W, Hu Y, Jiang Y. Experimental and theoretical investigation of ethyl methyl carbonate/air flames: Laminar burning velocity and cellular instability at elevated pressures. Fuel 2023;346:128206.
[14] Bauwens CR, Bergthorson JM, Dorofeev SB. Experimental study of spherical-flame acceleration mechanisms in large-scale propane–air flames. Proc Combust Inst 2015;35(2):2059–66.
[15] Bauwens CRL, Bergthorson JM, Dorofeev SB. Experimental investigation of spherical-flame acceleration in lean hydrogen-air mixtures. Int J Hydrogen Energy 2017;42(11):7691–7.
[16] Yang S, Saha A, Wu F, Law CK. Morphology and self-acceleration of expanding laminar flames with flame-front cellular instabilities. Combust Flame 2016;171:112–8.
[17] Ranga Dinesh KKJ, Shalaby H, Luo KH, van Oijen JA, Thévenin D. Effects of pressure on cellular flame structure of high hydrogen content lean premixed syngas spherical flames: A DNS study. Int J Hydrogen Energy 2016;41(46):21516–31.
[18] Han Z, Xiao B, Tian W, Li J, Yu W. Study on difference and adaptability of calculation method of spherical flame radius. Fuel 2020;259:116216.
[19] Du Y-L, Sun ZY, Huang Q, Sun Y-C. Observation study on the flame morphology of outwardly propagating turbulent HCNG-30 premixed flames. Int J Hydrogen Energy 2023;48(19):7096–114.
[20] Zuo Z, Hu B, Bao X, Zhang S, Fan L, Deng L, et al. Self-acceleration characteristics of premixed C1–C3 alkanes-air mixtures in a constant-volume chamber. Fuel Process Technol 2022;231:107252.
[21] Zuo Z, Hu B, Bao X, Zhang S, Kong L, Deng L, et al. Quantitative research on cellular instabilities of premixed C1–C3 alkane–air mixtures using spherically expanding flames. Fuel Process Technol 2022;226:107075.
[22] Yin G, Hu E, Li X, Lv X, Huang Z. Laminar Flame Instability of n-Hexane, n-Octane, and n-Decane in Spherical Expanding Flames. J Therm Sci 2024.
[23] Bao Y, Li X, Xu C, Wang Q, Oppong F. Experimental and theoretical study of 2-ethylfuran spherical expanding flame: Cellularization, intrinsic instability and self-acceleration. Fuel Process Technol 2022;238:107521.
[24] Xu C, Bao Y, Li X, Qian L, Oppong F. Pressure fluctuation and cellularization characteristics of 2-ethylfuran spherical expanding flame. Fuel 2023;349:128627.
[25] Scherr T, Seiffarth J, Wollenhaupt B, Neumann O, Schilling MP, Kohlheyer D, et al. microbeSEG: A deep learning software tool with OMERO data management for efficient and accurate cell segmentation. PLoS One 2022;17(11):e0277601.
[26] Liu P, Li J, Chang J, Hu P, Sun Y, Jiang Y, et al. Software Tools for 2D Cell Segmentation. Cells 2024;13(4).
[27] Stringer C, Wang T, Michaelos M, Pachitariu M. Cellpose: a generalist algorithm for cellular segmentation. Nat Methods 2021;18(1):100–6.
[28] Pachitariu M, Stringer C. Cellpose 2.0: how to train your own model. Nat Methods 2022;19(12):1634–41.
[29] Maška M, Ulman V, Delgado-Rodriguez P, Gómez-de-Mariscal E, Nečasová T, Guerrero Peña FA, et al. The Cell Tracking Challenge: 10 years of objective benchmarking. Nat Methods 2023;20(7):1010–20.
[30] Kim W, Imamura T, Mogi T, Dobashi R. Experimental investigation on the onset of cellular instabilities and acceleration of expanding spherical flames. Int J Hydrogen Energy 2017;42(21):14821–8.
[31] Wu H, Zheng J, Dong X, Zhang S, Ding Y. Investigations on the cellular instabilities of expanding hydrogen/methanol spherical flame. Int J Hydrogen Energy 2021;46(67):33601–15.
[32] Jiang Y-H, Li G-X, Li F-S, Sun Z-Y, Li H-M. Experimental investigation of correlation between cellular structure of the flame front and pressure. Fuel 2017;199:65–75.
[33] Xu H. Key Findings In 'MF and DMF - Engine Performance'; 2017. Available from: https://www.birmingham.ac.uk/research/activity/mechanical-engineering/case-centre/vehicle-technology/future-power/mf-and-dmf-engine-performance/key-findings.aspx [accessed January 10 2024].
[34] Huang S, Zhang Y, Huang R, Xu S, Ma Y, Wang Z, et al. Quantitative characterization of crack and cell's morphological evolution in premixed expanding spherical flames. Energy 2019;171:161–9.
[35] Huang S, Huang R, Zhang Y, Zhou P, Wang Z, Yin Z. Relationship between cellular morphology and self-acceleration in lean hydrogen-air expanding flames. Int J Hydrogen Energy 2019;44(59):31531–43.
[36] Li X, Wang Q, Oppong F, Liu W, Xu C. Cellularization characteristics of ethyl acetate spherical expanding flame. Fuel 2021;291:120213.
[37] Xu C, Wang Q, Li X, Oppong F, Liu W. The effect of intrinsic instability on the surface topography of spherical 2-acetylfuran flame. Fuel 2022;318:123624.
[38] Xu C, Liu W, Oppong F, Wang Q, Sun Z-Y, Li X. Investigations on cellularization instability of 2-ethylfuran. Renew Energy 2022;191:447–58.
[39] Xie Y, Elsayed Morsy M, Li J, Yang J. Intrinsic cellular instabilities of hydrogen laminar outwardly propagating spherical flames. Fuel 2022;327:125149.
[40] Stringer C. A generalist algorithm for cellular segmentation with human-in-the-loop capabilities; 2023. Available from: https://github.com/MouseLand/cellpose [accessed January 10 2024].
[41] Zhang G, Xu H, Wu D, Yang J, Morsy ME, Jangi M, et al. Deep learning-driven analysis for cellular structure characteristics of spherical premixed hydrogen-air flames. Int J Hydrogen Energy 2024;68:63–73.
[42] Han S, Phasouk K, Zhu J, Fong Y. Optimizing deep learning-based segmentation of densely packed cells using cell surface markers. BMC Med Inform Decis Mak 2024;24(1):124.
[43] Han Z, Hu M, Xu L, Zuo Z, Fang J, Wu Y, et al. Method for calculating spherical expanding flame radius considering the ignition electrode's influence. Fuel Process Technol 2024;256:108074.
[44] Zhou M, Li G, Zhang Z, Liang J, Tian L. Effect of Ignition Energy on the Initial Propagation of Ethanol/Air Laminar Premixed Flames: An Experimental Study. Energy Fuel 2017;31(9):10023–31.
[45] Xie Y, Elsayed Morsy M, Yang J. Self-Acceleration and global pulsation of unstable laminar Hydrogen-Air flames. Fuel 2023;353:129182.
[46] Wang D, Ji C, Wang S, Yang J, Tang C. Experimental investigation on near wall ignited lean methane/hydrogen/air flame. Energy 2019;168:1094–103.
[47] Askari O, Elia M, Ferrari M, Metghalchi H. Cell formation effects on the burning speeds and flame front area of synthetic gas at high pressures and temperatures. Appl Energy 2017;189:568–77.